

# Towards Top-Down Just Noticeable Difference Estimation of Natural Images

Qiuping Jiang, Zhentao Liu, Shiqi Wang, Feng Shao, and Weisi Lin, *Fellow, IEEE*

**Abstract**—Just noticeable difference (JND) of natural images refers to the maximum change magnitude that the typical human visual system (HVS) cannot perceive. Existing efforts on JND estimation mainly dedicate to modeling the visibility masking effects of different factors in spatial and frequency domains, and then fusing them into an overall JND estimate. However, the overall visibility masking effect can be related with more contributing factors beyond those have been considered in the literature and it is also insufficiently accurate to formulate the masking effect even for an individual factor. Moreover, the potential interactions among different masking effects are also difficult to be characterized with a simple fusion model. In this work, we turn to a dramatically different way to address these problems with a top-down design philosophy. Instead of formulating and fusing multiple masking effects in a bottom-up way, the proposed JND estimation model directly generates a critical perceptual lossless (CPL) image from a top-down perspective and calculates the difference map between the original image and the CPL image as the final JND map. Given an input image, an adaptively critical point (perceptual lossless threshold), defined as the minimum number of spectral components in Karhunen-Loéve Transform (KLT) used for perceptual lossless image reconstruction, is derived by exploiting the convergence characteristics of KLT coefficient energy. Then, the CPL image can be reconstructed via inverse KLT according to the derived critical point. Finally, the difference map between the original image and the CPL image is calculated as the JND map. The performance of the proposed JND model is evaluated with two applications including JND-guided noise injection and JND-guided image compression. Experimental results have demonstrated that our proposed JND model can achieve better performance than several latest JND models.

**Index Terms**—Just noticeable distortion, distortion visibility, masking effect, critical perceptual lossless, Karhunen-Loéve Transform.

## I. INTRODUCTION

Just noticeable difference (JND) refers to the maximum change magnitude that typical human visual system (HVS) cannot perceive. It reveals the visibility limitation of the HVS and reflects the underlying perceptual redundancy in visual signals, rendering it useful in many perceptual image/video processing applications such as image/video compression [1–4], perceptual image/video enhancement [5, 6], information hiding and watermarking [7–13], and visual quality assessment [14–18], etc. Due to its wide applications, JND estimation of

Q. Jiang, Z. Liu, and F. Shao are with the School of Information Science and Engineering, Ningbo University, Ningbo 315211, China (e-mail: {liuzhentao,jiangqiuping,shaofeng}@nbu.edu.cn).

S. Wang is with the Department of Computer Science, City University of Hong Kong, Kowloon Tong, Hong Kong (e-mail: shiqwang@cityu.edu.hk).

W. Lin is with the School of Computer Science and Engineering, Nanyang Technology University, Singapore (e-mail: wslin@ntu.edu.sg).

natural images has received much attention and been widely investigated. Generally, the JND models can be divided into two categories: JND models in pixel domain and JND models in frequency domain.

JND models in pixel domain directly calculate the JND at pixel level with considerations of either/both luminance adaption (LA) or/and contrast masking (CM) effects of the HVS. As the pioneering work, Chou *et al.* [19] first proposed a spatial-domain JND model by combining LA and CM. Afterwards, Yang *et al.* [20] further proposed a generalized spatial JND model with a nonlinear additivity model for masking effects (NAMM) to characterize the possible overlaps between LA and CM. Based on Yang et al.’s work, Liu *et al.* [21] introduced an enhanced pixel-level JND model with an improved scheme for CM estimation. Specifically, the image is first decomposed into structural component (i.e., cartoon like, piecewise smooth regions with sharp edges) and textural component using a total-variation algorithm. Then, the structural and textural components are used estimating EM and TM effects, respectively. In order to differently manipulate order and disorder regions, Wu *et al.* [22] designed a novel JND estimation model based on the free-energy principle. An autoregressive model is first applied to predict the order and disorder contents of an input image, then different schemes are used to estimate the JND threshold of these two parts, respectively. Further, Wu *et al.* [23] took the concept of pattern complexity (PC) into account for JND estimation. They quantified the pattern complexity as the diversity of pixel orientations. Finally, pattern masking is deduced and combined with the traditional CM for JND estimation. Jakhetiya *et al.* [24] further combines RMS contrast with LA and CM to build a more comprehensive JND model in low-frequency regions. For high-frequency regions, a feedback mechanism is used to efficiently mitigate the over- and under-estimations of CM. Chen *et al.* [25] took horizontal-vertical anisotropy and vertical-meridian asymmetry into consideration to yield a better JND estimation. The basic consideration is that the effect of eccentricity on visual sensitivity is not homogeneous across the visual field. Shen *et al.* [26] decompose the image into three components namely luminance, contrast, and structure. Since the masking of structure visibility (SM) is unknown, they trained a deep learning-based structural degradation estimation model to approximate SM. Finally, LA, CM and SM are combined to estimate the overall JND. Wang *et al.* [27] proposed a novel JND estimation model by exploiting the hierarchical predictive coding theory. They simulated both the positive and negative perception effects of each stage individually and integrated them with Yang’s

NAMM model [20] to yield the total JND threshold.

JND models in frequency domain firstly transform the original image into a specific transform domain and then the corresponding JND thresholds for each sub-band are estimated. The main consideration of these frequency domain-based JND models is to make use of the well-known contrast sensitivity function (CSF) which reflects the bandpass characteristics of HVS in the spatial frequency domain and is typically modeled as an exponential function of the spatial contrast [28]. In [29], the visibility thresholds for different frequencies are measured through subjective tests, and the CSF is built to account for the fundamental/base JND threshold for each sub-band. Typically, the JND thresholds for each sub-band are usually estimated based on a fixed size block (e.g.,  $8 \times 8$ ) via a linear combination of CSF and some other modulation factors. For example, Wei and Ngan [30] utilized a simple piecewise function to represent LA and formulated the CM as a categorizing function according to the richness of block texture information. Bae *et al.* [31] proposed a new DCT-based JND profile by incorporating the CSF, LA, and CM effects. Specifically, a new CM JND is modeled as a function of DCT frequency and a newly proposed structural contrast index (a new texture complexity metric that considers not only contrast intensity, but also structureness of image patterns). Wan *et al.* [32] analyzed orientation information with the DCT coefficients and a more accurate CM model was proposed in the DCT domain. Besides LA and CM, some works also considered foveated masking as influential factors for JND estimation. The foveated masking was first modeled by Chen *et al.* in [25] where it was utilized as an explicit form in pixel-domain JND and then incorporated in the frequency-domain JND estimation.

In general, the existing pixel-domain and frequency-domain JND models share the same design philosophy, i.e., modeling the visibility masking effects of different factors and then combining them together to derive an overall JND estimation. Such design philosophy can be considered as a bottom-up strategy which starts from the bottom concrete contributing factors and then progressively form the final estimation. However, this design philosophy has some inherent drawbacks. First, without having a deep understanding of the HVS properties, it is hard to take all the relevant contributing factors into account. Second, the masking modeling of different factors usually depends on some ideal assumptions or fitted on the data obtained from subjective experiments with controlled conditions. Obviously, the masking models/functions obtained in this way cannot be sufficiently accurate. Third, the potential interactions among different masking effects cannot be well characterized. Therefore, the performance of the existing JND estimation models is limited to achieve satisfactory results. Although we can make efforts to explore more contributing factors and try to model their corresponding visibility masking effects more accurately, such effort may be endless because new challenges always raise, i.e., how to characterize the possible interactions between different masking effects.

Given the above mentioned drawbacks of bottom-up design philosophy for JND estimation, we in this paper turn to a dramatically different way to address these problems with a

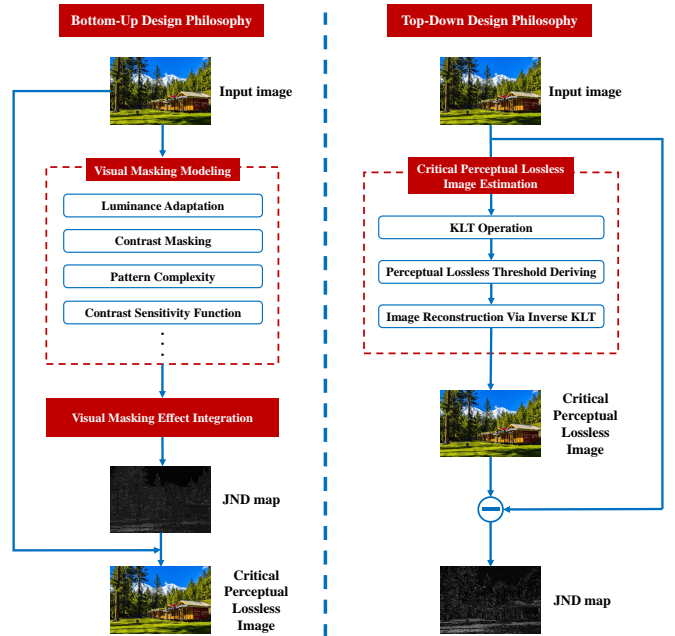


Fig. 1: Pipelines of bottom-up and top-down design philosophies for JND estimation.

top-down design philosophy. Keeping in mind that the goal is to estimate the maximum change magnitude (JND threshold) of each pixel that typical HVS cannot perceive. In other words, with an ideal JND map, if the original image is changed within the JND threshold, we can still perceive the changed image as a perceptual lossless one. With this in mind, we intuitively come up with the idea to directly generate a critical perceptual lossless (CPL) image from the original one and then calculate the difference between them to serve as the JND map, thus bypassing the inaccurate formulation and integration of different masking effects. **The CPL image refers to a changed image whose change magnitude is just at the critical point beyond which this changed image will be either perceived as lossy or not the critical one (although perceptual lossless).** Interestingly, though this idea is quite intuitive, it has not been touched in this field as far as we have known. To facilitate comparing the bottom-up and top-down design philosophies for JND estimation, we illustrate their pipelines in Fig. 1. As shown, our proposed top-down JND estimation (right column) first starts from the generation of a CPL image from the original one and then deduces the final JND map by calculating their difference. However, the traditional bottom-up JND estimation (left column) first starts from the formulation and integration of different masking effects to derive the overall JND map based on which a perceptual lossless image is expected to be obtained (the final result may not be perceptual lossless since the JND map established in this way may not be sufficiently accurate in fact).

Given an input image, we first perform the Karhunen-Loéve Transform (KLT) and then derive its critical point (i.e., perceptual lossless threshold) by exploiting the convergence characteristics of KLT coefficient energy. Once the critical

point is determined, the CPL image is reconstructed via inverse KLT. Then, the difference map between the original image and the CPL image is deemed as the visually redundant information that cannot be perceived by typical HVS and thus implies the visibility limitation of the HVS. Finally, we just simply take the derived difference map as the final JND map for more efficient and effective human visibility threshold estimation. Two kinds of experiments including JND-guided noise injection and JND-guided image compression are conducted to demonstrate the superiority of the proposed JND model over several latest JND models. While keeping almost the same visual quality, our proposed JND model can guide to hide more noises and save more bit rates.

Our proposed top-down JND is also different with the picture-wise JND concept. In [33], Jin et al. conducted subjective experiments to find the JND point (i.e., the quality factor (QF) in JPEG compression) for a given image. In their experiments, an input image is compressed by the JPEG encoder 100 times with the quality factor (QF) set ranging from 1 to 100. Then, each volunteer is asked to find the quality transition point between the best quality level (original image) and the second best quality level. This quality transition point is called the first JND point. Thus, the JND point is just a specific QF value. However, in our proposed method, the critical point is a specific index of spectral component in KLT. As we will demonstrate later, different spectral components in KLT are responsible for different parts of visual information in an image. Compared with the QF value which is mainly applicable to image compression applications, the index of spectral component in KLT is not restricted to any specific applications and thus the JND model build based on KLT is more general and applicable to diverse applications. In addition, in [33], it only constructed such a database containing pristine images and the associated JND points (QFs) while no JND estimation model is developed.

At the end of this section, we summarize the main contributions of this work as follows:

1) We propose an novel JND model for natural images with a top-down design philosophy that bypasses the inaccurate formulation and integration of different masking effects for more efficient and effective human visibility threshold estimation. This new top-down pipeline will shed new light on future research on JND estimation.

2) We transfer the problem of JND estimation into estimating a CPL counterpart from its original version and resort to the KLT to derive the critical point by exploiting the convergence characteristics of KLT coefficient energy. With the determined critical point, the CPL image is reconstructed via inverse KLT.

3) We conduct experiments to demonstrate the superiority of the proposed JND models over several latest JND models on JND-guided noise injection and JND-guided image compression. While maintaining almost the same visual quality, the proposed JND profile can guide to hide more noise and save more bit rates.

The rest of this paper is organized as follows. Section II illustrates our JND profile, including our design philosophy, motivation, and the details of our new JND profile based on

CPL derivation. Section III presents the experimental results and comparisons with state-of-the-art JND profiles. Finally, conclusions are drawn in section IV.

## II. METHODOLOGY

### A. Design Philosophy and Motivation

As stated, we turn to a top-down design philosophy for JND estimation. As illustrated in Fig. 1, most of the traditional JND profiles follow a bottom-up design philosophy. Given an input image, they start from visibility masking effect modeling of multiple factors including LA, CM, PC, CSF, etc. Afterwards, those masking effects are fused together to obtain a final JND estimation via linear or nonlinear combinations. However, this bottom-up design philosophy suffers from some inherent drawbacks. First, the overall visibility masking effect of the HVS can be related with more contributing factors beyond those have been considered in the existing works and it is also insufficiently accurate to formulate the masking effect even for a single specific contributing factor. Moreover, the used linear or nonlinear models for different masking effect fusion are also unable to characterize the complex interactions among different masking effects. To overcome such drawbacks, we propose a top-down design philosophy.

Considering the visibility limitation of HVS, it is believed that a CPL counterpart of the input image exists. **The CPL image refers to a changed image whose change magnitude is just at the critical point beyond which this changed image will be either perceived as lossy or not the critical one (although perceptual lossless).** Since we just cannot perceive the difference in the CPL, thus the difference map between the original image and the CPL image is just the JND map according to the definition of JND. **Thus, the problem of JND estimation can be transferred into a CPL image estimation problem.** Compared with directly estimating the JND map, it is much easier and intuitive to derive a CPL image. In this work, we resort to the KLT to obtain the CPL image.

KLT is a signal-dependent linear transform. As a data-driven transform, it KLT has been applied in image coding [34], image quality assessment [35, 36] and achieved promising results due to its excellent decorrelated performance. The KLT domain and spatial domain can be converted from one to another without loss of information. Given an input image, we first transfer it from the spatial domain to the KLT domain. The KLT coefficients associated with different spectral components are responsible for visual information in different aspects. The former spectral components are responsible for macro-structures image information while the latter spectral components are responsible for micro-structures image information. To validate this point, Fig. 2 illustrates the image reconstruction process via inverse KLT, i.e., from KLT domain to spatial domain, with different numbers of spectral components. In this example, we set the total number of spectral components  $K = 64$ . Fig. 2(a) is the original image, Fig. 2(b)-(h) are the reconstructed images with the first  $k$  spectral components, where  $k \in \{1, 2, 4, 8, 16, 32, 64\}$ . As shown in Fig. 2(b), when only the 1-st spectral component is involved for reconstruction,

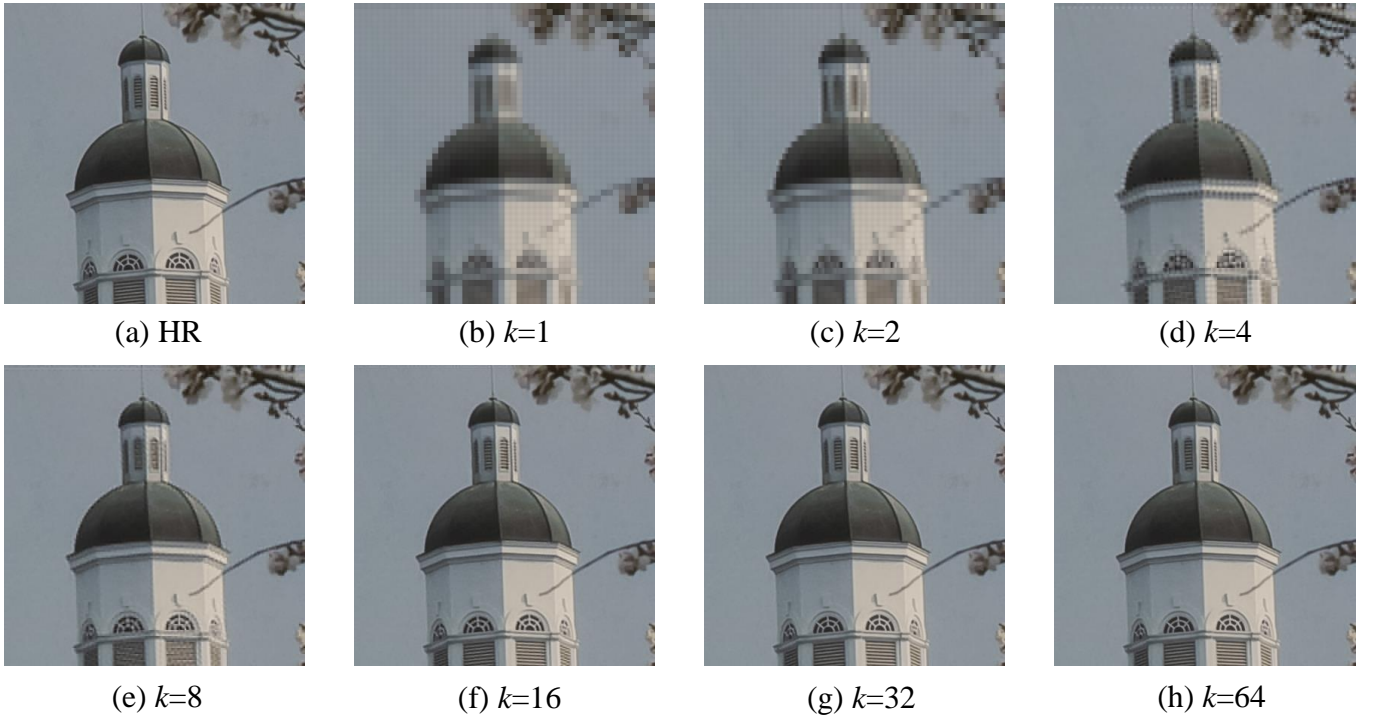


Fig. 2: Reconstructed images with different numbers of spectral components via inverse KLT.

almost all the macro-structures are recovered. However, many small textures and fine details are missing. As  $k$  increases, the small textures and fine details become richer and clearer. These observations well validate our previous statement that different spectral components are responsible for image information in different aspects. Generally, we have the insight that the front part of spectral components in the KLT coefficient matrix take charge of the reconstruction of image macro-structures such as the basic contour and main structures while the latter part of spectral components take charge of the reconstruction of image micro-structures such as the textures and fine details.

Obviously, there is a redundancy of visual information in an image. As shown in Fig. 2(f), when we take the first 16 spectral components to perform reconstruction via inverse KLT, the visual quality of the reconstructed image is almost the same with that of the original image, i.e., Fig. 2(a). The image reconstruction process via inverse KLT demonstrates that some micro-structure image information is perceptually redundant to HVS and directly discard the corresponding spectral components in the KLT coefficient matrix for reconstruction would not cause visible visual quality degradation of the reconstructed image. We wonder that if there exists a critical point (perceptual lossless threshold)  $L$  which satisfies the following property: when we take the first  $L$  spectral components to perform image reconstruction via inverse KLT, all the macro-structure image information and sufficient micro-structure image information are recovered so as to reconstruct the CPL image. Obviously, the accurate determination of the critical point  $L$  is a key step to the success of our JND model as different critical points  $L$  will yield different CPL images as well as different JND maps.

### B. JND Profile Based on CPL Image Estimation

1) *Image Transform Using KLT*: KLT is a signal dependent linear transform, the kernels of which are derived by computing the principal components along eigen-directions of the autocorrelation matrix of the input data. Given an image  $\mathbf{X}$  with size  $M \times N$ , a set of non-overlapping patches with size  $\sqrt{K} \times \sqrt{K}$  are extracted. These image patches are vectorized and combined together to form a new matrix  $\mathbf{X} = [\mathbf{x}_1, \mathbf{x}_2, \dots, \mathbf{x}_S] \in \mathbb{R}^{K \times S}$ , where  $\mathbf{x}_s \in \mathbb{R}^{K \times 1}$ ,  $s = 1, 2, \dots, S$  represents the  $s$ -th vectorized patch and  $S$  is the total number of image patches in  $\mathbf{X}$ . The covariance matrix of  $\mathbf{X}$  is defined as follows

$$\mathbf{C} = \mathbb{E}[(\mathbf{x}_s - \bar{\mathbf{x}})(\mathbf{x}_s - \bar{\mathbf{x}})^T] \quad (1)$$

$$= \frac{1}{S-1} \sum_{s=1}^S (\mathbf{x}_s - \bar{\mathbf{x}})(\mathbf{x}_s - \bar{\mathbf{x}})^T \quad (2)$$

where  $\bar{\mathbf{x}} = \frac{1}{S} \sum_{s=1}^S \mathbf{x}_s$  denotes the mean vector obtained by averaging each row of  $\mathbf{X}$  and  $\mathbf{C} \in \mathbb{R}^{K \times K}$ . Then, the eigenvalues and eigenvectors of  $\mathbf{C}$  are calculated via eigenvalue decomposition. The eigenvectors are arranged according to their corresponding eigenvalues in the descending order to form the KLT kernel  $\mathbf{P} = [\mathbf{p}_1, \mathbf{p}_2, \dots, \mathbf{p}_K] \in \mathbb{R}^{K \times K}$  where  $\mathbf{p}_k \in \mathbb{R}^{K \times 1}$ ,  $k = 1, 2, \dots, K$  represents the  $k$ -th eigenvector. Using the KLT kernel  $\mathbf{P}$ , the KLT of  $\mathbf{X}$  is expressed as follows:

$$\mathbf{Y} = \mathbf{P}^T \mathbf{X} \quad (3)$$

where  $\mathbf{Y} = [\mathbf{y}_1, \mathbf{y}_2, \dots, \mathbf{y}_K]^T \in \mathbb{R}^{K \times S}$  is the KLT coefficient matrix and  $\mathbf{y}_k \in \mathbb{R}^{S \times 1}$ ,  $k = 1, 2, \dots, K$  refers to the  $k$ -th spectral component obtained by  $\mathbf{y}_k = (\mathbf{p}_k)^T \mathbf{X}$ .

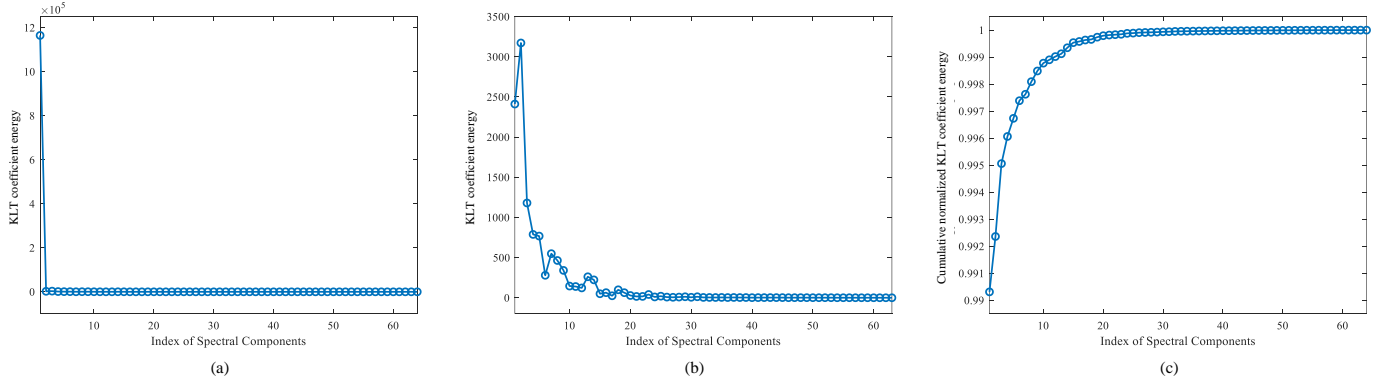


Fig. 3: Distribution curve of the normalized KLT coefficient energy and cumulative normalized KLT coefficient energy.

2) *Convergence Property of KLT Coefficient Energy*: After obtaining the KLT coefficient matrix  $\mathbf{Y}$ , we calculate the KLT coefficient energy  $E_k$  for spectral component  $y_k$  as follows:

$$E_k = \frac{1}{S} \sum_{s=1}^S \mathbf{Y}(k, s)^2, \quad k = 1, 2, \dots, K. \quad (4)$$

In order to remove the influence of image content, we further calculate the normalized KLT coefficient energy  $p_k$  as follows:

$$p_k = \frac{E_k}{E_1 + E_2 + \dots + E_K}, \quad k = 1, 2, \dots, K. \quad (5)$$

Fig. 3(a) shows the normalized KLT coefficient energy distribution curve for the image in Fig. 2(a). Since  $p_1$  is particularly large than others, we further plot another curve in Fig. 3(b) by excluding  $p_1$ . As shown in Fig. 3(b), as the spectral component index  $k$  increases, the KLT coefficient energy  $p_k$  first drops dramatically and later converges to be stable. When  $k$  is larger than 20,  $p_k$  becomes extremely small and gradually converges to zero. This phenomenon is consistent with the inverse KLT-based image reconstruction process illustrated in Fig. 2. The former spectral components occupy much larger energies than the later ones so that they take charge of the macro-structure image information. The latter spectral components own relatively small energies such that they are in charge of the micro-structure image information.

Now, let us take a look at the normalized KLT coefficient energy curve from an cumulative perspective. The cumulative normalized KLT coefficient energy  $P_k$  is defined as follows:

$$P_k = p_1 + p_2 + \dots + p_k, \quad k = 1, 2, \dots, K. \quad (6)$$

The cumulative distribution curve of the normalized KLT coefficient energy for the image in Fig. 2(a) has been shown in Fig. 3(c). Note that  $P_1 = p_1$  and has been already close to 1 due to the particularly large energy of the first spectral component. As  $k$  increases,  $P_k$  monotonously increases. When  $k > 20$ ,  $P_k$  will gradually converges to 1, indicating the recovered visual information gradually become saturated.

3) *Critical Point Derivation*: For images with different contents, although their cumulative distribution curves have the same convergence tendency, their critical points that lead to sufficient visual information may be different, as demonstrated in Fig. 4. Therefore, it is required to design an adaptive scheme

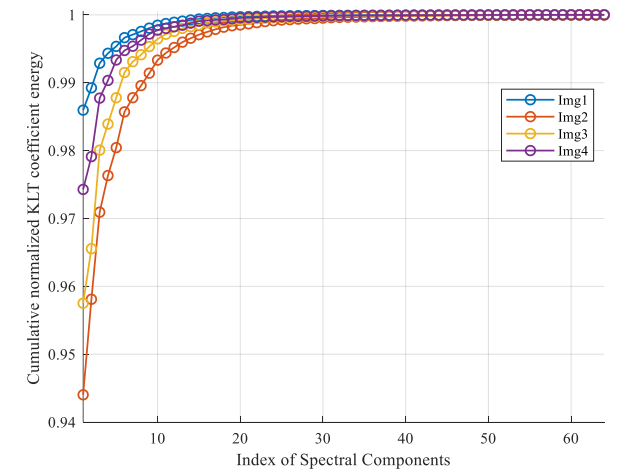
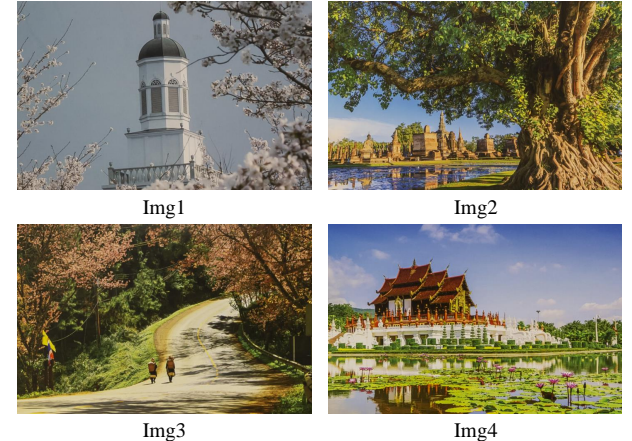


Fig. 4: Cumulative distribution curve of the normalized KLT coefficient energy.

to automatically determine the critical point for different images. In the following, we will illustrate how this issue is addressed with subjective studies and statistical analyses.

We select a total number of 500 high visual quality images from the DIV2K [37, 38] dataset. For each image, we apply the KLT-based image transform and inverse KLT-based image reconstruction with the first  $k$  spectral components,  $k = 1, 2, \dots, K$ . Thus, we can obtain  $K$  reconstructed images

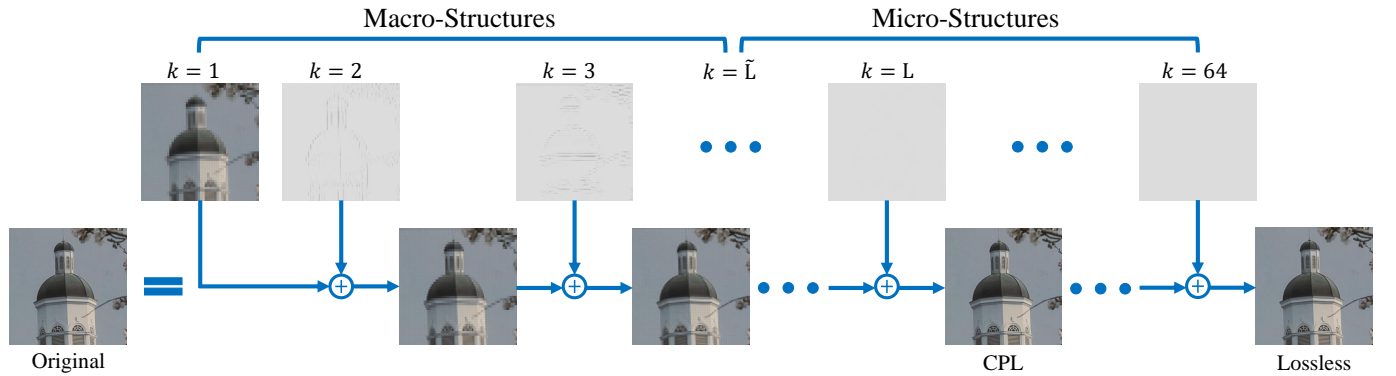


Fig. 5: Visualization of the progressive image reconstruction process via inverse KLT.

for each original image. Then, we conduct a user study to subjectively determine the critical point  $L \in \{1, 2, \dots, K\}$  for each original image. Details of the user study are illustrated as follows.

There are 60 subjects participated in our experiment. Each subject  $s^m$  is asked to compare each original image  $I_o$  and its corresponding  $K$  reconstructed versions  $\{I_r^k\}$  one-by-one. Specifically, the image pairs are presented in a pre-defined order:  $\{I_o, I_r^1\}, \{I_o, I_r^2\}, \dots, \{I_o, I_r^K\}$ . Then, each subject observes the presented image pairs carefully and give a binary judgment to answer the question whether the presented image pair has visible difference or not. Typically, subjects will observe obvious difference for the first several image pairs and then gradually have difficulties in differentiating the later ones. For each subject, the user study will stop once this subject cannot observe any visible difference from a certain image pair  $\{I_o, I_r^k\}$  and we consider this spectral component index  $k$  as the critical point given by the  $m$ -th subject  $s^m$  for the  $n$ -th original image  $I_o^n$ :  $I_o^n: L_n^m = k$ .

Let us denote the critical points given by all subjects for the  $n$ -th original image as  $\mathbf{L}_n = [L_n^1, L_n^2, \dots, L_n^{60}]$ . Then, we remove the outlier data points from  $\mathbf{L}_n$  according to the well-known Pauta criterion which assumes that a set of test data only contains random errors, calculate it to obtain standard deviation, and determine a range according to a certain probability of 99.7% [39]. It is considered that the error exceeding this interval is not a random error but a coarse error. That is, a specific element  $L_n^m$  will be excluded if it does not satisfy  $\mu_{\mathbf{L}_n} - 3\sigma_{\mathbf{L}_n} \leq L_n^m \leq \mu_{\mathbf{L}_n} + 3\sigma_{\mathbf{L}_n}$  where  $\mu_{\mathbf{L}_n}$  and  $\sigma_{\mathbf{L}_n}$  denote the mean value and standard deviation of  $\mathbf{L}_n$ , respectively. After outlier removal,  $\mathbf{L}_n$  will be updated to be  $\mathbf{L}'_n$ . We further calculate the mean value  $\mu_{\mathbf{L}'_n}$  and set the final critical point for the  $n$ -th original image as follows:

$$L_n = \lceil \mu_{\mathbf{L}'_n} \rceil, \quad (7)$$

where  $\lceil \cdot \rceil$  represents the round up operation.

Next, we calculate the corresponding cumulative KLT coefficient energy  $P_{L_n}$  for each original image with the obtained critical points  $L_n \in \{1, 2, \dots, K\}$ . As a result, we can obtain a vector  $\mathbf{P}_L = [P_{L_1}, P_{L_2}, \dots, P_{L_{500}}]$  with each element representing the critical cumulative KLT coefficient energy of a specific original image. To have a better understanding on  $\mathbf{P}_L$ , we calculate the mean value  $\mu_{\mathbf{P}_L}$  and standard deviation

$\sigma_{\mathbf{P}_L}$  of  $\mathbf{P}_L$  to simply characterize the distributions of  $\mathbf{P}_L$ . Specifically,  $\mu_{\mathbf{P}_L}$  indicates the average level of critical cumulative KLT coefficient energy over all image samples when the visual quality of the reconstructed images achieve converging while  $\sigma_{\mathbf{P}_L}$  indicates the variation range. For a specific input image  $X$ , if the cumulative KLT coefficient energy  $P_k$  falls into the range  $[\mu_{\mathbf{P}_L} - 3\sigma_{\mathbf{P}_L}, \mu_{\mathbf{P}_L} + 3\sigma_{\mathbf{P}_L}]$ , we think that all the macro-structure image information and sufficient micro-structure image information can be recovered and the visual quality converges. Thus, we can determine the critical point  $L$  of an input image as follows:

$$L = \arg \min_k k, \quad s.t. \quad \mu_{\mathbf{P}_L} - 3\sigma_{\mathbf{P}_L} \leq P_k \leq \mu_{\mathbf{P}_L} + 3\sigma_{\mathbf{P}_L}. \quad (8)$$

The estimated critical point  $L$  is closely related with the redundancy of visual information. When we take the first  $L$  spectral components for image reconstruction via inverse KLT, it is expected to generate the CPL counterpart of the original image. In what follows, we will illustrate how the CPL image can be reconstructed with the first  $L$  spectral components.

4) *CPL Image Reconstruction*: To utilize the first  $L$  spectral components for image reconstruction via inverse KLT, we first define the corresponding reconstruction KLT coefficient matrix  $\mathbf{Y}^{(L)}$  as follows:

$$\mathbf{Y}^{(L)} = \begin{bmatrix} y_{1,1} & \cdots & y_{L,1} & 0 & \cdots & 0 \\ \vdots & \ddots & \vdots & \vdots & \ddots & \vdots \\ y_{1,S} & \cdots & y_{L,S} & 0 & \cdots & 0 \end{bmatrix}^T \quad (9)$$

where  $\mathbf{Y}^{(L)} \in \mathbb{R}^{K \times S}$ ,  $k = 1, 2, \dots, K$ . Then, the image is reconstructed as follows:

$$\mathbf{X}^{(L)} = \mathbf{P} \mathbf{Y}^{(L)} \quad (10)$$

where  $\mathbf{X}^{(L)}$  represents the reconstructed image by only considering the first  $k$  spectral components. Since  $L$  is the estimated critical point,  $\mathbf{X}^{(L)}$  can be considered as the CPL image.

Fig. 5 visualizes the progressive image reconstruction process. In this example, we set  $K = 64$ . The images shown in the top row are the reconstructed results using only each individual single spectral component while the images shown in the bottom row are the reconstructed results using all previous spectral components. It is obvious that only using the first spectral component for reconstruction could recover

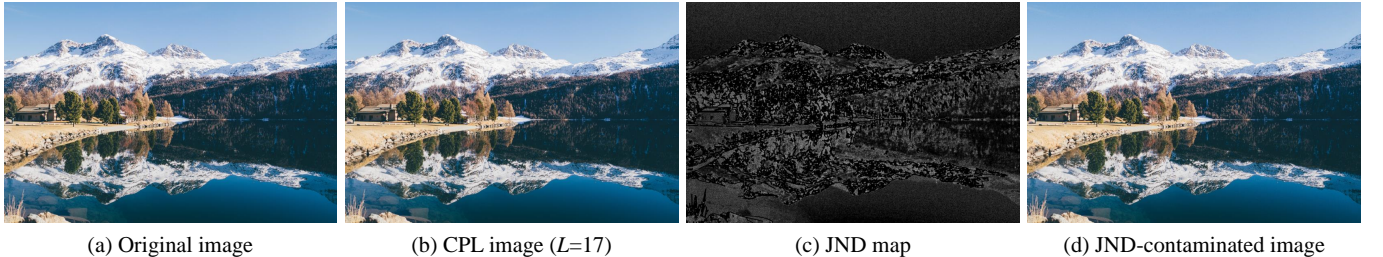


Fig. 6: An example of noise contaminated image guided by our JND map. The PSNR value of the contaminated image shown in (d) is 26dB.

most macro-structures of the original image. When more spectral components are involved, the image is progressively reconstructed with richer and finer details. Suppose  $\tilde{L}$  is the boundary between macro- and micro-structures. Using the former  $\tilde{L}$  spectral components will successfully reconstruct all the macro-structures and the latter ( $64 - \tilde{L}$ ) spectral components will mainly responsible for the reconstruction of micro-structures. For the critical point  $L$  we have estimated, it means that we at least need to use the former  $L$  spectral components to reconstruct all the macro-structures and sufficient micro-structures required for a perceptual lossless image. Finally, if all the spectral components are involved, the original image can be completely reconstructed without any information loss.

5) *JND Map*: Once the CPL image  $\mathbf{X}^{(L)}$  is obtained, we compute the difference map between the original image  $\mathbf{X}$  and  $\mathbf{X}^{(L)}$  as the final JND map  $\mathbf{M}$ :

$$\mathbf{M}(i, j) = |\mathbf{X}(i, j) - \mathbf{X}^{(L)}(i, j)|, \quad (11)$$

where  $|\cdot|$  denotes the absolute value operator,  $i, j$  are the pixel coordinates in spatial domain.

### III. EXPERIMENTS

In this section, the proposed JND model is compared with the existing JND models to demonstrate its accuracy and efficiency. Specifically, the JND model is used to guide noise injection and image compression. We will present these two experiments one-by-one in the following.

#### A. Performance of JND-Guided Noise Injection

The performance of a JND model can be measured by the capability of hiding noise. Specifically, we can get the JND-contaminated image by injecting random noise into the image with the guidance of the estimated JND map as follows:

$$\tilde{\mathbf{X}}(i, j) = \mathbf{X}(i, j) + \theta \cdot \mathbf{N}(i, j) \cdot \mathbf{M}(i, j), \quad (12)$$

where  $\tilde{\mathbf{X}}$  is the JND-contaminated image,  $\mathbf{N}$  denotes the bipolar random noise of  $\pm 1$ , and  $\theta$  is a noise energy regulating factor. By adjusting the value of  $\theta$ , the amount of noise injected into the image can be well controlled. In other words, we can inject almost the same amount of noise into the test image (almost the same PSNR) by adjusting the value of  $\theta$  for different JND maps.

In Fig. 6, we give an example to show the results of nosie contaminated image guided by our proposed JND map.



Fig. 7: The original images used in the experiments.

Obviously, it is difficult to perceive the visual quality difference between the original image (i.e., Fig. 6(a)) and the noise-contaminated image (i.e., Fig. 6(d)). That is, although the PSNR value is only 26dB, the injected noise cannot be perceived in the noise-contaminated image guided by our proposed JND map. From the JND map shown in Fig. 6(c), we notice that many details in the complex textured regions are redundant to the HVS. Using such a JND map as a guidance for noise injection, the contaminated image will be perceived with high quality since most of the noises are encouraged to be added in those highly redundant area that is not visible to the HVS.

Apparently, with the guidance of a more accurate JND map, the JND-contaminated image (obtained by Eq. (12)) with same noise level should have better visual quality. As stated, for different JND models, we can adjust the value of  $\theta$  in Eq. (12) to ensure that almost the same amount of noise is injected. Then, the performance of a JND model can be evaluated by measuring the MS-SSIM [41] score and the mean opinion score (MOS) of the obtained noise-contaminated image. MS-SSIM is a popular full-reference image quality metric that is measured between the original image and the contaminated image. Theoretically, the MS-SSIM score falls in the range  $[0, 1]$  and a higher MS-SSIM score indicates better visual quality. The MOS score is obtained via subjective assessment experiments. Another 30 subjects are invited to participate the subjective experiments. Each subject is asked to assign an opinion score in the range  $[-1, 0]$  to a specific image pair including one original image and one JND-contaminated

TABLE I: Performance Comparison of JND-based Noise Injection.

Method	Yang2005 [20]		Zhang2005 [40]		Wu2013 [22]		Wu2017 [23]		Jahetiya2018 [24]		Chen2020 [25]		Proposed	
Image	MS-SSIM	MOS	MS-SSIM	MOS	MS-SSIM	MOS	MS-SSIM	MOS	MS-SSIM	MOS	MS-SSIM	MOS	MS-SSIM	MOS
I01	0.9744	-0.8333	0.9766	-0.6333	0.9768	-0.6000	0.9796	-0.5667	0.9818	-0.5778	0.9740	-0.3889	<b>0.9823</b>	<b>-0.3222</b>
I02	0.9736	-0.6444	0.9763	-0.7222	0.9840	-0.4667	0.9821	-0.3889	0.9859	-0.3778	0.9683	-0.6222	<b>0.9871</b>	<b>-0.1556</b>
I03	0.9592	-0.6556	0.9547	-0.7333	0.9594	-0.6000	0.9706	-0.5333	0.9642	-0.5889	0.9577	-0.6778	<b>0.9737</b>	<b>-0.2333</b>
I04	0.9580	-0.5556	0.9494	-0.7111	0.9579	-0.5111	0.9705	-0.3556	0.9680	-0.4111	0.9378	-0.8222	<b>0.9792</b>	<b>-0.1889</b>
I05	0.9269	-0.7111	0.9305	-0.6222	0.9306	-0.5778	0.9437	-0.4222	0.9407	-0.4444	0.9268	-0.5889	<b>0.9685</b>	<b>-0.1889</b>
I06	0.9511	-0.6222	0.9545	-0.5444	0.9635	-0.5000	0.9698	-0.3556	0.9721	-0.3889	0.9356	-0.7222	<b>0.9780</b>	<b>-0.2556</b>
I07	0.9691	-0.6333	0.9615	-0.6333	0.9710	-0.5222	0.9775	-0.4111	0.9798	-0.3556	0.9453	-0.7111	<b>0.9798</b>	<b>-0.2444</b>
I08	0.9603	-0.4778	0.9577	-0.5778	0.9628	-0.5222	0.9742	-0.2889	0.9721	-0.5667	0.9488	-0.7222	<b>0.9817</b>	<b>-0.2333</b>
I09	0.9506	-0.5667	0.9375	-0.6444	0.9397	-0.5333	0.9588	-0.3778	0.9522	-0.4889	0.9274	-0.7444	<b>0.9732</b>	<b>-0.2667</b>
I10	0.9524	-0.6000	0.9525	-0.6667	0.9545	-0.5222	0.9642	-0.4111	0.9644	-0.3444	0.9501	-0.5333	<b>0.9694</b>	<b>-0.2889</b>
I11	0.9453	-0.6000	0.9330	-0.6000	0.9368	-0.4778	0.9569	-0.3000	0.9489	-0.4000	0.9215	-0.7222	<b>0.9742</b>	<b>-0.2778</b>
I12	0.9435	-0.4333	0.9450	-0.4000	0.9461	-0.3444	0.9569	-0.3778	0.9593	-0.3000	0.9411	<b>-0.2778</b>	<b>0.9749</b>	-0.4778
I13	0.9820	-0.5556	0.9777	-0.5778	0.9824	-0.4778	0.9846	-0.3667	0.9849	-0.4000	0.9643	-0.6778	<b>0.9855</b>	<b>-0.3222</b>
I14	0.9676	-0.3667	0.9590	-0.4667	0.9678	-0.4111	0.9775	-0.3000	0.9682	-0.4889	0.9423	-0.7889	<b>0.9805</b>	<b>-0.2667</b>
I15	0.9508	-0.4111	0.9475	-0.4889	0.9546	-0.4222	0.9634	-0.3000	0.9613	-0.4556	0.9421	-0.7444	<b>0.9740</b>	<b>-0.2222</b>
I16	0.9386	-0.3333	0.9304	-0.5333	0.9345	-0.5000	0.9529	-0.3444	0.9493	-0.3778	0.9242	-0.6333	<b>0.9723</b>	<b>-0.2444</b>
I17	0.9583	-0.4222	0.9470	-0.6222	0.9561	-0.4667	0.9723	-0.3111	0.9624	-0.4000	0.9422	-0.6778	<b>0.9793</b>	<b>-0.2111</b>
I18	0.9561	-0.4222	0.9518	-0.5444	0.9622	-0.3778	0.9743	-0.2333	0.9718	-0.3000	0.9372	-0.6333	<b>0.9818</b>	<b>-0.2111</b>
I19	0.9539	-0.3778	0.9501	-0.5889	0.9614	-0.4333	0.9701	-0.3222	0.9678	-0.3778	0.9395	-0.7111	<b>0.9785</b>	<b>-0.2444</b>
I20	0.9470	-0.3778	0.9325	-0.5444	0.9397	-0.4667	0.9596	-0.2889	0.9538	-0.3667	0.9160	-0.6333	<b>0.9794</b>	<b>-0.2444</b>
Average	0.9567	-0.5300	0.9515	-0.5928	0.9579	-0.4867	0.9688	-0.3628	0.9665	-0.4206	0.9414	-0.6517	<b>0.9783</b>	<b>-0.2550</b>

image. Note that the two images are juxtaposed a 65-in monitor at left and right with random order for comparison. A score equals to 0 means the visual quality of the JND-contaminated image is equal to that of the original image while a score equal to -1 means the visual quality of the JND contaminated image is dramatically worse than that of the original image. As a result, for each contaminated image, 30 scores are collected from all subjects. After removing the outlier, the mean value of the retained opinion scores is calculated as the MOS. A more accurate JND model will result in higher MS-SSIM score and MOS than the competitors while their PSNR values are almost the same (the same noise level).

We select 20 high-quality images from the DIV2K [37, 38] dataset as the original images in the experiments. These images are shown in Fig. 7. The proposed JND model is compared with six existing JND models including Yang2005 [20], Zhang2005 [40], Wu2013 [22], Wu2017 [23], Jakhetiya2018 [24], and Chen2020 [25]. Note that all these compared JND models are designed based on the bottom-up design philosophy while the proposed one is the only top-down JND model as far as we have known. The detailed performance results of different JND models on noise injection are shown in Table I. As shown in Table I, our JND model achieves the best performance in MS-SSIM for all the images, and the best performance in MOS for all the images except the image ‘I12’. In addition, our proposed JND model achieves the best performance in both MS-SSIM and MOS at an average level when considering all the images. These experimental results demonstrate the superiority of our proposed JND method against others in guiding noise injection.

In order to make a more clear comparison among these JND models, Fig. 8 gives a visual example of the JND maps and the noise contaminated images. Images in the first row are the original image (‘I03’) and different JND maps whose pixel values are mapped into [0, 255] for better visualization. Images in the second row are the original image and noise contaminated images generated by using different JND models as guidance according to Eq. (12). By adjusting the parameter  $\theta$ , the PSNR values of these noise-contaminated images are controlled to be almost the same ( $26 \pm 0.02$ dB). Images in the third row are the enlarged versions of the sub-regions cropped from the images in the second column. As shown in Fig. 8, we can observe that the noise-contaminated image guided by our proposed JND model is the ‘cleanest’ one among all the compared ones. It seems that Fig. 8(h) is perceptually the same with the original image (Fig. 8(a)) as it does not contain any visible noise. Among the competitors, Fig. 8(e) also has achieved acceptable visual quality while it is still worse than Fig. 9(h). With careful observations, one can still perceive visible noise in the sky area of Fig. 8(e).

By taking a closer look at Fig. 8(h), one can find that the injected noises are hidden in those textured areas such as the walls and leaves. However, it is hard to be perceived by the HVS at the first glance. As has been reported in [23], the HVS is highly adapted to extracting the repeated patterns for visual content representation and it is hard to perceive the noise which is injected into the textured areas with high pattern complexity. By contrast, it is much easier for the HVS to perceive the noise in those relatively smooth or flat areas. Compared with the smooth/flat areas, textured



Fig. 8: Visual comparison of noise-contaminated images generated by using different JND models as guidance.

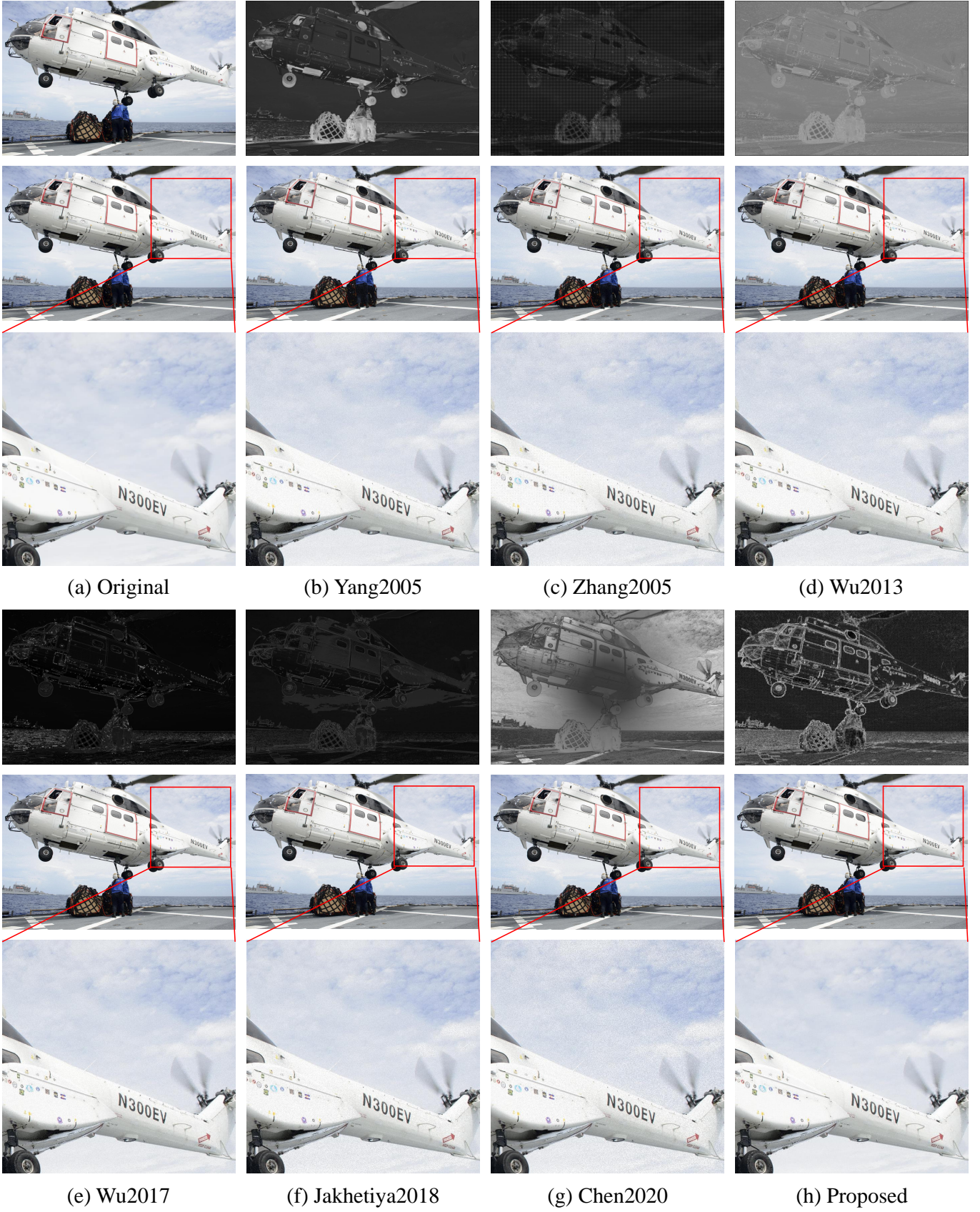


Fig. 9: Visual comparison of noise-contaminated images generated by using different JND models as guidance.

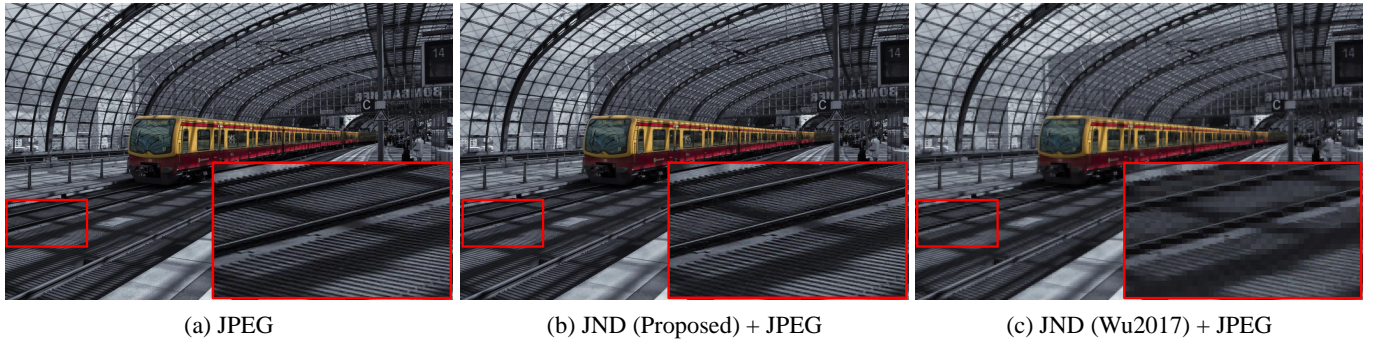


Fig. 10: Visual quality comparison of JND-guided image compression. (a) Direct JPEG compression result of image “I01”; (b) Our proposed JND model-guided JPEG compression result of image “I01”; (c) Wu2017 JND model-guided JPEG compression result of image “I01”.

areas tend to contain much more details (e.g., micro-structures) and are likely to be redundant. As we have demonstrated before, the difference map between the original image and the derived CPL image can well resemble the redundant micro-structure image information to the HVS. Thus, our proposed JND model using such difference map as the JND map will encourage to hide the noise in those highly redundant areas. Therefore, the injected noises will not be easily visible by the HVS. What’s more, instead of modeling and aggregating the masking effects of diverse contributing factors in isolation, our proposed JND model dedicates to deriving a CPL image to best exploit the potential perceptual redundancies exist in the original image from a top-down perspective. Thus, our proposed JND model would be able to implicitly characterize the influence of more potential factors beyond those have been considered in the literature. As a result, our proposed JND model can generate a perceptually better noise contaminated image than the existing ones. Another visual example is shown in Fig. 9. The original image is “I09” and the PSNR of all the noise-contaminated images is also set to  $26 \pm 0.02$ dB. Again, the noise-contaminated image guided by our JND model (Fig. 9(h)) achieves the best visual quality.

### B. Performance of JND-Guided Image Compression

The JND map implies the visibility limitation of the HVS. Thus, it is often employed in image compression to improve coding efficiency. Generally, the smoothing operation can reduce the signal variance, which makes image compression easier. However, blindly smoothing operations will always jeopardize image quality. Thus, we in this experiment use the JND map to guide the smoothing operation as a preprocess step before JPEG compression for perceptual redundancy reduction. As will be illustrated later, the visual quality of the compressed image guided by our proposed JND model will not be affected too much while saving considerable coding bits. Specifically, given an input image  $\mathbf{T}$  and its corresponding JND map  $\mathbf{T}_M$ , the JND-guided image smoothing operation is described as follows:

$$\tilde{\mathbf{T}}(i, j) = \begin{cases} \mathbf{T}(i, j) + \mathbf{T}_M(i, j), & \mathbf{T}(i, j) - \bar{\mathbf{T}}_P < -\mathbf{T}_M(i, j) \\ \mathbf{T}(i, j) - \mathbf{T}_M(i, j), & \mathbf{T}(i, j) - \bar{\mathbf{T}}_P > \mathbf{T}_M(i, j) \\ \bar{\mathbf{T}}_P, & \text{else} \end{cases} \quad (13)$$

where  $\bar{\mathbf{T}}_P$  denotes the mean value of the block that  $\mathbf{T}(i, j)$  belongs to during the compression process (e.g., the divided  $8 \times 8$  blocks that  $\mathbf{T}(i, j)$  located at during JPEG compression).

With the above JND-guided image smoothing operation, the visual redundancy of the input image will be significantly reduced to optimize the compression. One visual example is shown in Fig. 10 where we perform JPEG compression of the original image “I01” at QP=1 in two different ways: direct JPEG compression and JND-guided JPEG compression. Fig. 10(a) is the result obtained by direct JPEG compression. Fig. 10(b) is the result obtained by first preprocessing the original image with the JND-guided image smoothing operation and then performing JPEG compression. It can be observed that, though less bit rate is required (0.0684 bpp for Fig. 10(a) and 0.0595 bpp for Fig. 10(b)), the visual quality of Fig. 10(b) is almost equal to that of Fig. 10(a). As a comparison, we also provide the result obtained by using Wu2017 JND model as the guidance under the same JPEG compression QP. As shown in Fig. 10(c), though the bit rate of Fig. 10(c) is 0.0362 bpp which is less than Fig. 10(c), we can easily perceive obvious compression artifact in this result.

As illustrated in Fig. 10, we notice that in comparison with Fig. 10(c), Fig. 10(b) achieves higher visual quality at the cost of higher bit rate. Therefore, an important issue is how to fairly compare the overall performance of different JND-guided JPEG compression results. The key is to jointly take visual quality and bit rate into account by using a single performance criteria. Keeping this in mind, we define the gain  $G = \frac{\Delta \text{Bitrate}}{\Delta \text{PSNR}}$  as the criteria, where  $\Delta \text{Bitrate}$  denotes the saving of bit rate and  $\Delta \text{PSNR}$  denotes the reduction of PSNR value. Specifically, these two measures are calculated as follows:  $\Delta \text{Bitrate} = \frac{\text{Bitrate}_{\text{ori}} - \text{Bitrate}_{\text{jnd}}}{\text{Bitrate}_{\text{ori}}} \times 100\%$  and  $\Delta \text{PSNR} = \frac{\text{PSNR}_{\text{ori}} - \text{PSNR}_{\text{jnd}}}{\text{PSNR}_{\text{ori}}} \times 100\%$ , where  $\text{Bitrate}_{\text{ori}}$  and  $\text{PSNR}_{\text{ori}}$  represent the bit rate and PSNR value of direct JPEG compressed image, respectively,  $\text{Bitrate}_{\text{jnd}}$  and  $\text{PSNR}_{\text{jnd}}$  represent the bit rate and PSNR value of JND-guided JPEG compressed image, respectively. According this definition, it is reasonable to say a higher value of  $G$  indicates a better performance of a JND model for guiding the JPEG compression. We thus evaluate the performance of JND-guided JPEG compression using  $G$  and show the results in Table II.

TABLE II: Performance Comparison of JND-Guided JPEG Compression (QP=1).

Image	JND (Proposed) + JPEG			JND (Wu2017) + JPEG		
	$\Delta B$ itrate	$\Delta P$ SNR	G	$\Delta B$ itrate	$\Delta P$ SNR	G
I01	13.06%	4.20%	<b>3.1102</b>	47.12%	17.46%	2.6988
I02	8.16%	2.45%	<b>3.3332</b>	39.64%	29.68%	1.3357
I03	25.71%	5.41%	<b>4.7532</b>	42.74%	11.30%	3.7819
I04	19.70%	4.73%	<b>4.1646</b>	43.47%	13.89%	3.1287
I05	31.37%	7.10%	<b>4.4179</b>	43.89%	12.51%	3.5099
I06	11.12%	2.41%	<b>4.6151</b>	38.10%	12.62%	3.0183
I07	13.32%	3.93%	<b>3.3864</b>	38.60%	15.07%	2.5610
I08	17.80%	6.19%	<b>2.8771</b>	44.82%	17.93%	2.4996
I09	17.45%	7.17%	<b>2.4358</b>	35.16%	15.98%	2.2006
I10	25.01%	5.32%	<b>4.7009</b>	46.94%	14.29%	3.2859
I11	22.67%	10.46%	2.1668	37.34%	16.35%	<b>2.2839</b>
I12	14.74%	5.31%	<b>2.7771</b>	44.10%	20.35%	2.1671
I13	16.01%	4.46%	<b>3.5893</b>	43.88%	14.37%	3.0536
I14	28.66%	4.95%	<b>5.7901</b>	51.00%	11.93%	4.2754
I15	19.32%	3.10%	<b>6.2258</b>	45.15%	13.19%	3.4214
I16	20.15%	6.99%	<b>2.8818</b>	36.45%	15.75%	2.3143
I17	28.23%	5.68%	<b>4.9666</b>	46.18%	12.35%	3.7384
I18	18.40%	3.49%	<b>5.2660</b>	45.34%	11.78%	3.8485
I19	23.14%	3.25%	<b>7.1273</b>	47.82%	8.98%	5.3267
I20	23.59%	5.89%	<b>4.0061</b>	39.94%	12.24%	3.2626
Average	19.88%	5.12%	<b>3.8795</b>	42.88%	14.90%	2.8779

As shown in Table II, our proposed JND model-guided JPEG compression is able to save 19.88% of bitrates in average while Wu2017's JND model-guided JPEG compression can save 42.88% of bitrates in average. However, our proposed JND model-guided JPEG compression only reduces 5.12% of PSNR value in average while Wu2017's JND model-guided JPEG compression will reduce 14.90% of PSNR value in average. By taking PSNR reduction and bitrate saving into account simultaneously with a single criteria  $G$ , our proposed JND model-guided JPEG compression achieves much larger values of  $G$  for the majority images (except "I11") and also a much larger average value of  $G$  when considering all the images together. We further adjust the QP values and draw the curves of the average value of  $G$  with different QP values, as depicted in Fig. 11. Our proposed JND model-guided JPEG compression consistently owns higher average value of  $G$  than that of Wu2017's by a large margin at each QP value. This further demonstrates the superiority of our proposed JND model for improving the efficiency of JPEG compression. Based on these experimental results, we can safely conclude that: 1) in comparison with the direct JPEG compression, the JPEG compression guided by our proposed JND model could further save moderate bitrates while without reducing the visual quality too much; 2) in comparison with Wu2017's JND model, JPEG compression guided by our proposed JND model could achieve a much better balance between visual quality reduction and bit rate saving, i.e., a much higher value of  $G$ .

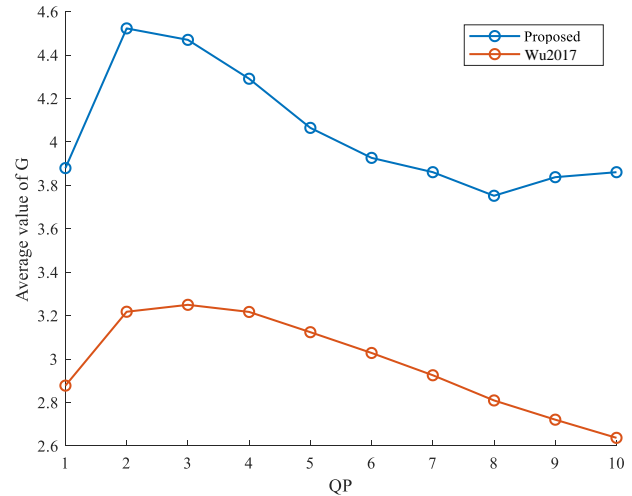


Fig. 11: The average value of  $G$  with different QP values in JPEG compression.

#### IV. CONCLUSION

This paper has presented a novel top-down JND estimation model of natural images. It dedicates to estimating a CPL image first by exploiting the convergence characteristics of the KLT coefficient energy and then calculating the difference map between the original image and CPL image as the JND map. The difference map well reflects the redundant micro-structure information which typically cannot be perceived by the HVS. Using such a difference map as the final JND map, the visual redundancies in the image can be better exploited. Since the proposed JND model does not require the inaccurate and incomplete formulation of the masking effects of different contributing factors, it no longer suffers from the drawbacks of the existing bottom-up JND estimation models, and thus a better performance can be achieved. We have evaluated the performance of the proposed JND model with two applications: JND-guided noise injection and JND-guided image compression. Experimental results have demonstrated that our proposed JND model can achieve better performance than several latest JND models on both tasks.

#### REFERENCES

- [1] H. R. Wu, A. R. Reibman, W. Lin, F. Pereira, and S. S. Hemami, "Perceptual visual signal compression and transmission," *Proceedings of the IEEE*, vol. 101, no. 9, pp. 2025–2043, 2013.
- [2] X. Zhang, S. Wang, K. Gu, W. Lin, S. Ma, and W. Gao, "Just-noticeable difference-based perceptual optimization for jpeg compression," *IEEE Signal Processing Letters*, vol. 24, no. 1, pp. 96–100, 2017.
- [3] C.-M. Mak and K. N. Ngan, "Enhancing compression rate by just-noticeable distortion model for h.264/avc," in *2009 IEEE International Symposium on Circuits and Systems*, 2009, pp. 609–612.
- [4] X. Yang, W. Ling, Z. Lu, E. Ong, and S. Yao, "Just noticeable distortion model and its applications in video coding," *Signal Processing: Image Communication*, vol. 20, no. 7, pp. 662–680, 2005.
- [5] S.-W. Jung, J.-Y. Jeong, and S.-J. Ko, "Sharpness enhancement of stereo images using binocular just-noticeable difference," *IEEE Transactions on Image Processing*, vol. 21, no. 3, pp. 1191–1199, 2012.

[6] W. Lin, Y. Gai, and A. Kassim, "Perceptual impact of edge sharpness in images," in *IEE Proceedings of Vision, Image and Signal Processing*, vol. 152, pp. 215–223, 05 2006.

[7] C.-H. Chou and K.-C. Liu, "A perceptually tuned watermarking scheme for color images," *IEEE Transactions on Image Processing*, vol. 19, no. 11, pp. 2966–2982, 2010.

[8] Y. Niu, J. Liu, S. Krishnan, and Q. Zhang, "Combined just noticeable difference model guided image watermarking," in *2010 IEEE International Conference on Multimedia and Expo*, 2010, pp. 1679–1684.

[9] Y. Niu, M. Kyan, L. Ma, A. Beghdadi, and S. Krishnan, "Visual saliency's modulatory effect on just noticeable distortion profile and its application in image watermarking," *Signal Processing: Image Communication*, vol. 28, no. 8, pp. 917–928, 2013.

[10] M. Bouchakour, G. Jeannic, and F. Autrusseau, "Jnd mask adaptation for wavelet domain watermarking," in *2008 IEEE International Conference on Multimedia and Expo*, 2008, pp. 201–204.

[11] Q. Cheng and T. Huang, "An additive approach to transform-domain information hiding and optimum detection structure," *IEEE Transactions on Multimedia*, vol. 3, no. 3, pp. 273–284, 2001.

[12] Z. Fu, K. Ren, J. Shu, X. Sun, and F. Huang, "Enabling personalized search over encrypted outsourced data with efficiency improvement," *IEEE Transactions on Parallel and Distributed Systems*, vol. 27, no. 9, pp. 2546–2559, 2016.

[13] X. Chen, G. Gao, D. Liu, and Z. Xia, "Steganalysis of lsb matching using characteristic function moment of pixel differences," *China Communications*, vol. 13, no. 7, pp. 66–73, 2016.

[14] W. Lin and C.-C. Jay Kuo, "Perceptual visual quality metrics: A survey," *Journal of Visual Communication and Image Representation*, vol. 22, no. 4, pp. 297–312, 2011.

[15] S. A. Fezza, M.-C. Larabi, and K. M. Faraoun, "Stereoscopic image quality metric based on local entropy and binocular just noticeable difference," in *2014 IEEE International Conference on Image Processing (ICIP)*, 2014, pp. 2002–2006.

[16] S. Wang, D. Zheng, J. Zhao, W. J. Tam, and F. Speranza, "Adaptive watermarking and tree structure based image quality estimation," *IEEE Transactions on Multimedia*, vol. 16, no. 2, pp. 311–325, 2014.

[17] J. Wu, W. Lin, G. Shi, and A. Liu, "Reduced-reference image quality assessment with visual information fidelity," *IEEE Transactions on Multimedia*, vol. 15, no. 7, pp. 1700–1705, 2013.

[18] S. Seo, S. Ki, and M. Kim, "A novel just-noticeable-difference-based saliency-channel attention residual network for full-reference image quality predictions," *IEEE Transactions on Circuits and Systems for Video Technology*, vol. 31, no. 7, pp. 2602–2616, 2021.

[19] C.-H. Chou, "A perceptually tuned subband image coder based on the measure of just-noticeable-distortion profile," in *Proceedings of 1994 IEEE International Symposium on Information Theory*, 1994, pp. 420–.

[20] X. Yang, W. Lin, Z. Lu, E. Ong, and S. Yao, "Motion-compensated residue pre-processing in video coding based on just-noticeable-distortion profile," *IEEE Transactions on Circuits and Systems for Video Technology*, vol. 15, no. 6, pp. 742–752, 2005.

[21] A. Liu, W. Lin, M. Paul, C. Deng, and F. Zhang, "Just noticeable difference for images with decomposition model for separating edge and textured regions," *IEEE Transactions on Circuits and Systems for Video Technology*, vol. 20, no. 11, pp. 1648–1652, 2010.

[22] J. Wu, G. Shi, W. Lin, A. Liu, and F. Qi, "Just noticeable difference estimation for images with free-energy principle," *IEEE Transactions on Multimedia*, vol. 15, no. 7, pp. 1705–1710, 2013.

[23] J. Wu, L. Li, W. Dong, G. Shi, W. Lin, and C.-C. J. Kuo, "Enhanced just noticeable difference model for images with pattern complexity," *IEEE Transactions on Image Processing*, vol. 26, no. 6, pp. 2682–2693, 2017.

[24] V. Jakhetiya, W. Lin, S. Jaiswal, K. Gu, and S. C. Guntuku, "Just noticeable difference for natural images using rms contrast and feed-back mechanism," *Neurocomputing*, vol. 275, pp. 366–376, 2018.

[25] Z. Chen and W. Wu, "Asymmetric foveated just-noticeable-difference model for images with visual field inhomogeneities," *IEEE Transactions on Circuits and Systems for Video Technology*, vol. 30, no. 11, pp. 4064–4074, 2020.

[26] X. Shen, Z. Ni, W. Yang, X. Zhang, S. Wang, and S. Kwong, "Just noticeable distortion profile inference: A patch-level structural visibility learning approach," *IEEE Transactions on Image Processing*, vol. 30, pp. 26–38, 2021.

[27] H. Wang, L. Yu, J. Liang, H. Yin, T. Li, and S. Wang, "Hierarchical predictive coding-based jnd estimation for image compression," *IEEE Transactions on Image Processing*, vol. 30, pp. 487–500, 2021.

[28] J. Wu, G. Shi, and W. Lin, "A survey of visual just noticeable difference estimation," *Front. Comput. Sci.*, 2019.

[29] Y. Jia, W. Lin, and A. Kassim, "Estimating just-noticeable distortion for video," *IEEE Transactions on Circuits and Systems for Video Technology*, vol. 16, no. 7, pp. 820–829, 2006.

[30] Z. Wei and K. N. Ngan, "Spatio-temporal just noticeable distortion profile for grey scale image/video in dct domain," *IEEE Transactions on Circuits and Systems for Video Technology*, vol. 19, no. 3, pp. 337–346, 2009.

[31] S.-H. Bae and M. Kim, "A novel generalized dct-based jnd profile based on an elaborate cm-jnd model for variable block-sized transforms in monochrome images," *IEEE Transactions on Image Processing*, vol. 23, no. 8, pp. 3227–3240, 2014.

[32] W. Wan, J. Wu, X. Xie, and G. Shi, "A novel just noticeable difference model via orientation regularity in dct domain," *IEEE Access*, vol. 5, pp. 22 953–22 964, 2017.

[33] L. Jin, J. Y. Lin, S. Hu, H. Wang, P. Wang, I. Katsavounidis, A. Aaron, and C.-C. J. Kuo, "Statistical study on perceived jpeg image quality via mcl-jci dataset construction and analysis," *Electronic Imaging*, vol. 2016, no. 13, pp. 1–9, 2016.

[34] X. Zhang, C. Yang, X. Li, S. Liu, H. Yang, I. Katsavounidis, S.-M. Lei, and C.-C. J. Kuo, "Image coding with data-driven transforms: Methodology, performance and potential," *IEEE Transactions on Image Processing*, vol. 29, pp. 9292–9304, 2020.

[35] C. Yang, X. Zhang, P. An, L. Shen, and C.-C. J. Kuo, "Blind image quality assessment based on multi-scale klt," *IEEE Transactions on Multimedia*, vol. 23, pp. 1557–1566, 2021.

[36] X. Zhang, S. Kwong, and C.-C. J. Kuo, "Data-driven transform based compressed image quality assessment," *IEEE Transactions on Circuits and Systems for Video Technology*, 2020.

[37] R. Timofte et al., "Ntire 2017 challenge on single image super-resolution: Methods and results," in *2017 IEEE Conference on Computer Vision and Pattern Recognition Workshops (CVPRW)*, 2017, pp. 1110–1121.

[38] E. Agustsson and R. Timofte, "Ntire 2017 challenge on single image super-resolution: Dataset and study," in *2017 IEEE Conference on Computer Vision and Pattern Recognition Workshops (CVPRW)*, 2017, pp. 1122–1131.

[39] Z. Yang, L. Tian, and C. Li, "A fast video shot boundary detection employing otsu's method and dual pauta criterion," in *2017 IEEE International Symposium on Multimedia (ISM)*, 2017, pp. 583–586.

[40] X. Zhang, W. Lin, and P. Xue, "Improved estimation for just-noticeable visual distortion," *Signal Processing*, vol. 85, no. 4, pp. 795–808, 2005.

[41] Z. Wang, E. P. Simoncelli, and A. C. Bovik, "Multiscale structural similarity for image quality assessment," in *The Thirty-Seventh Asilomar Conference on Signals, Systems Computers*, 2003, vol. 2, 2003, pp. 1398–1402 Vol.2.